Assessment of a clinically feasible Bayesian fitting algorithm using a simplified description of Chemical Exchange Saturation Transfer (CEST) imaging

In Journal of Magnetic Resonance

DOI: 10.1016/j.jmr.2019.01.006

Assessment of a clinically feasible Bayesian fitting algorithm using a simplified description of Chemical Exchange Saturation Transfer (CEST) imaging

Purpose: Chemical Exchange Saturation Transfer (CEST) contrast is based on the exchange of protons between metabolites and water. Fitting a model based on the Bloch-McConnell (BM) equations to CEST spectra allows for the quantification of underlying parameters such as metabolite concentration and exchange rate while simultaneously correcting for main field inhomogeneity, direct water saturation and magnetization transfer. Employing a Bayesian fitting approach permits the integration of prior information into the analysis to incorporate expected parameter distributions and to prevent over-fitting. However, the analysis can be time consuming if a general numerical solution of the BM equations is applied.

Methods: To achieve feasible computational times, we combined a Bayesian fitting algorithm with approximate analytical solutions of the BM equations. Simulated data, and data from Iodipamide and Taurine phantom measurements were fitted to evaluate the accuracy and speed of the suggested approach. Both continuous-wave (CW) and pulsed saturation with Gaussian pulses were considered.

Results: An about 50-fold reduction of computational time was measured when fitting CW data with the analytical model. For pulsed saturation data, the reduction was more than 100-fold. In most cases the estimated parameters did not differ significantly from the parameters estimated with the general numerical solution. In one case the analytical algorithm converged to the ground truth, while the general algorithm did not.

Conclusion: The increased speed of the algorithm facilitates the Bayesian analysis of CEST data within clinically feasible processing times. Other analytical models valid for different parameter regimes may be employed to extend the applicability to a wider range of CEST agents.

1. Introduction

Chemical Exchange Saturation Transfer (CEST) is an approach in magnetic resonance imaging (MRI) aiming to detect molecules containing exchangeable protons. The CEST contrast results from the selective saturation of these protons and their subsequent exchange with bulk water protons which in turn leads to a measurable reduction of the water signal. This CEST effect can be several orders of magnitude larger than the direct signal from the metabolites as measured with magnetic resonance spectroscopy (MRS) techniques, leading to enhanced sensitivity [1]. Various endogenous as well as exogenous CEST agents have been utilised in studies to investigate physiological parameters that are used as risk factors for the prediction of several pathologies[2–4]. For example, the endogenous CEST effect in Amide Proton Transfer (APT) imaging depends on the exchange rate of amide NH groups, which has been shown to be pH-dependent and capable of detecting pH deficits in stroke [5].

Several approaches have been adopted to quantify the CEST effect, such as, among others, the magnetization transfer ratio (MTR), the asymmetry magnetization transfer ratio (MTR_{asym}), quantitative CEST (qCEST) [6], the Omega plot [7], QUEST and QUESP (quantifying exchange rates using the saturation time and saturation power dependencies) [8] and

QUEST with ratiometric analysis (QUESTRA) [9]. In the case of MTR, the water proton signal S_{sat} which is obtained upon saturation at a single offset frequency is compared to the water signal without saturation S_0. However, MTR might be overestimated due a direct effect on the water signal known as the “spill-over effect”. This effect is often symmetric with respect to the water frequency and can therefore be eliminated by means of an additional reference measurement at the negative offset frequency, which is exploited for MTR_{asym}. A bias is introduced, however, if the reference measurement is influenced by non-symmetric effects caused by exchanging protons with overlapping resonance frequencies or slow exchange processes mediated via the Nuclear Overhauser Effect (NOE) [10]. Furthermore, these metrics quantify the magnitude of the CEST effect, but do not give much insight about the underlying parameters such as agent concentration or exchange rate. These parameters can be determined by qCEST, Omega plot, QUEST, QUESP and QUESTRA. In contrast to MTR and MTR_{asym}, many acquisitions with varying saturation parameters (i.e. variations of the length and/or amplitude of the saturation pulse) are typically required which can result in long scanning times.

CESTR* is another metric that has recently been developed [11] and which has potential to quantify pH differences between tumour and normal tissue *in vivo* without the need for exogenous contrast agents [12]. This metric is calculated based on parameters estimated by a Bayesian model-fitting method [13], which has previously been shown to permit the quantification of the APT effect *in vivo*, even in the presence of asymmetries in the Z-spectrum arising from Magnetization Transfer (MT) or NOE-mediated contributions [11].

In contrast to conventional least-squares fitting [14,15], Bayesian model-fitting of the Z-spectrum provides a framework to combine *prior* information about the model parameters with the information inferred from the measured data, also referred to as the *likelihood*. The prior information reflects the expected values and uncertainties for each model parameter such as information available from previous experiments. Furthermore, this approach reduces the risk of over fitting which can arise when a large number of model parameters is estimated from fitting data with a low signal-to-noise ratio (SNR).

One of the main limitations of the current Bayesian model-fitting approach for CEST is the long processing time which can be up to several hours per acquired section [11]. Especially in the clinic such long processing times are not feasible. The bottleneck of the algorithm is the evaluation of the model itself which is based on a numerical solution of the Bloch-McConnell (BM) equations [16,17].

On the other hand, analytical approximations of the BM equations which were shown to be valid for different ranges of physiological parameter values and experimental settings have been developed [18–23]. Here, we show that the processing time of the Bayesian model-fitting approach can be reduced considerably by replacing the BM equations with analytical approximations without significantly affecting the resulting parameter distributions or the convergence of the algorithm. We evaluated the modified algorithm by comparing the estimated parameters to those obtained from the algorithm based on the numerical solution of the BM equations. This evaluation was performed on both simulated data and data from the measurement of phantoms. The analytical approximations that were applied in this study were derived by Zaiss et al. [24] for CEST data acquired with continuous-wave

(CW) saturation and by Roeloffs et al. [22] for CEST data acquired with a pulsed saturation scheme. In the case of pulsed saturation, the analytical solution was further developed to be applicable to adiabatic Gaussian-shaped pulses.

2. Theory

Bayes theorem

Bayesian model-fitting is based on Bayes theorem which combines the prior distribution $p(\Theta)$ with the likelihood $p(S|\Theta)$ to obtain the posterior distribution $p(\Theta|S)$:

$$p(\Theta|S) \propto p(S|\Theta)p(\Theta). \tag{1}$$

The measured data is given by S and the set of N model parameters by $\Theta = \{\Theta_1, \dots, \Theta_i, \dots, \Theta_N\}$. Assuming a model $f(\Theta)$ and additive Gaussian noise with standard deviation σ_n, the likelihood can be expressed by the probability density function:

$$p(S|\Theta) = \frac{1}{\sigma_n\sqrt{2\pi}} e^{\frac{(S-f(\Theta))^2}{2\sigma_n^2}}. \tag{2}$$

In the context of CEST, S represents one or multiple measured Z-spectra and Θ corresponds to the set of model parameters to be estimated by the fitting algorithm such as exchange rates and equilibrium magnetizations. Furthermore, the model is given by a numerical or, as applied in this study, analytical solution of the BM equations.

Integrating the posterior distribution over all model parameters but one, Θ_i, renders the so-called marginalized posterior $p(\Theta_i|S)$ which reflects the estimated probability distribution for Θ_i. The mean of this distribution $\overline{p(\Theta_i|S)}$ can be interpreted as the expected value of Θ_i and credible intervals can be determined, e.g. the σ-credible interval corresponds to the range of values within which Θ_i falls with a probability of 0.68.

A Z-spectrum can be accurately described by a model $f(\Theta)$ which is based on the BM equations. If only one CEST agent is present a 2-pool-model with pool b describing the agent and pool a describing the bulk water can be applied. Each pool i is modelled by its longitudinal and transverse relaxation rates T_{1i} and T_{2i}, concentration M_{0i}, resonance frequency ω_i and forward proton exchange rate constant k_{ij} with pool j. A general numerical solution of the BM equations can be found in [25], however its evaluation is computationally demanding as it contains a matrix exponential [15]. Instead of the full model, two simplified approximations for the cases of CW saturation and pulsed saturation were applied here.

CW saturation

For CW saturation, the following approximate solution was used [24]:

$$Z(t) = (P_z P_{zeff} - Z_{\mathrm{CW}}^{\mathrm{SS}})\exp(-\mathrm{R}_{1\rho} t) + Z_{\mathrm{CW}}^{\mathrm{SS}}. \quad (3)$$

P_z and P_{zeff} are factors describing the projection of magnetization along the z-axis onto the direction of the effective magnetic field and vice versa. They are given by $P_z = P_{zeff} = \cos(\theta)$, where $\theta = \tan^{-1}\left(\frac{\omega_1}{\Delta\omega}\right)$ is the angle between the effective magnetic field and the z-axis. The parameters ω_1 and $\Delta\omega = \omega_{rf} - \omega_a$ designate the CW saturation amplitude and frequency offset with respect to the resonance frequency of the water pool. The steady-state value is given by

$$Z_{\mathrm{CW}}^{\mathrm{SS}} = \cos^2(\theta)\frac{R_{1a}}{R_{1\rho}}, \quad (4)$$

and the longitudinal relaxation rate of the water pool in the rotating frame, including the contribution due to chemical exchange, by $R_{1\rho}$. An approximate analytical expression for $R_{1\rho}$ is given in Appendix A.

Pulsed saturation

For pulsed saturation, we employ a solution termed ISAR2 derived in [22] for a series of n rectangular pulses of duration t_p, interleaved with delays of duration t_d, and here we extend it for the case of adiabatic Gaussian-shaped saturation pulses:

$$Z(n) = (Z_i - Z^{SS})\beta^n e^{-R_{1\rho}t_p n} + Z^{SS}, \tag{5}$$

where Z_i is the initial normalized water magnetization.

Furthermore:

$$\beta = P_{zeff}P_z(d_{aa} + d_{ab}\Psi) \tag{6}$$

and

$$Z^{\mathrm{SS}}_{\mathrm{pulsed}} = 1 - \frac{1 - P_z P_{z_{eff}}(f_b - \Psi)\exp(-R_{1\rho}t_p) - Z^{\mathrm{SS}}_{\mathrm{CW}}(1 - \exp(-R_{1\rho}t_p))}{1 - P_z P_{zeff}(d_{aa} + \Psi d_{ab})\exp(-R_{1\rho}t_p)}. \tag{7}$$

Expressions for d_{aa} and d_{ab} are given in Appendix B. The parameter Ψ represents the ratio of z-magnetizations of pool b and a at the end of the rectangular saturation pulse and can be expressed as:

$$\Psi = f_b(1 - \alpha_{lab}), \tag{8}$$

where α_{lab} is the labelling efficiency:

$$\alpha_{lab}(\Delta\omega) = \frac{R_{ex}(\Delta\omega)}{f_b k_{ba}}, \tag{9}$$

An analytical expression for the exchange-dependent relaxation rate R_{ex} is given by equation 13 in Appendix A.

Extension to Gaussian-shaped pulses

Equation 5 was derived for a train of rectangular pulses. In the following, we assume that shaped pulses can be treated in a similar manner as the integration of adiabatic spin-lock pulses [26,27]. To extend the ISAR2 approach for shaped pulses, reasonable assumptions for the parameters P_z and P_{zeff} , the effective $R_{1\rho}$ and the initial condition after the pulse given by Ψ have to be found.

1. Assumption: Shaped pulses are adiabatic. This is given if [28]: $\dot{\theta} \ll \omega_{eff}$. This allows the assumption $P_z = P_{zeff} = 1$.

2. Assumption: The effective $R_{1\rho}$ decay during the pulse can be described by the mean value $\overline{R_{1\rho}}$ given by:

$$\overline{R_{1\rho}} = \frac{1}{t_p}\int_{t=0}^{t_p} R_{1\rho}(\omega_1(t))dt\ . \tag{10}$$

3. Assumption: The parameter Ψ represents the ratio of magnetizations of pool b and a at the end of the pulse and is given by equation 8 when rectangular pulses are considered. However, if the envelope of the RF pulse varies slowly with respect to k_b, the magnetization of pool b is determined by the last B_1-value of the pulse, which is approximately 0 for a Gaussian shape. This corresponds to a labelling efficiency of $\alpha_{lab} = 0$. Thus, for fast exchange, Ψ should be replaced by f_b.

If the changes in the RF envelope are comparable to k_b the state of pool b becomes complicated, however Ψ must be somewhere between the upper bound $\Psi_{max} = f_b$ and a lower bound given by the value predicted for a block pulse with the same average $\overline{R_{ex}}$,

which is $\Psi_{min} = f_b - \frac{\overline{R_{ex}}}{k_b}$. As a first guess, Ψ is replaced by $\overline{\Psi} = f_b - \frac{\overline{R_{ex}}}{k_b}\alpha_{start}$, where α_{start} is introduced as a heuristic parameter ($0 < \alpha_{start} < 1$) that determines $\overline{\Psi}$ subject to $\Psi_{min} < \overline{\Psi} < \Psi_{max}$. For the Gaussian pulses employed in the following experiments, the value of $\alpha_{start} = 0.5$ was chosen based on numerical simulations of the Bloch-McConnell equations (see Appendix C).

3. Methods

The convergence of the algorithm and accuracy of determined fit parameters were investigated by fitting the simplified model equations to simulated as well as phantom data for both CW saturation (equation 3) and pulsed saturation (equation 5).

Simulation experiments

Z-spectra were simulated by evaluating the general solution of the BM equations numerically [15] in Matlab (vR2016b). For pulsed saturation, Gaussian-shaped pulses were approximated by piecewise constant pulses, i.e. each pulse was split into 200 uniform segments of constant pulse amplitude.

The simulation parameters describing the sample were chosen to represent typical values of APT phantoms. A two-pool model was assumed with one pool describing the amide proton and the other pool the water proton with the following parameters: $T_{1a} = 3s$, $T_{2a} = 1.5s$, $T_{1b} = 1s$, $T_{2b} = 0.015s$ and $k_{ba} = 30$Hz. The equilibrium magnetizations were assumed as $M_{0a} = 1$ and $M_{0b} = 0.007$ and the resonance frequency of the amide protons at 3.5ppm. The spectra were sampled at saturation frequency offsets $\Delta\omega_a$ from -6ppm to 6ppm in steps

of 0.1ppm. White Gaussian noise with a standard deviation of $\sigma = 0.02$ was added to all simulated spectra before the fitting procedure.

The parameter values of the pulse sequence and MRI scanner assumed for the CW saturation experiment were as follows: $B_0 = 7\text{T}$, $B_1 = 3.2\mu\text{T}$ and pulse duration $t_p = 10\text{s}$. The pulsed saturation experiment was simulated with: $B_0 = 7\text{T}$, $n = 50$ Gaussian pulses of duration $t_p = 0.1\text{s}$, standard deviation $\sigma_p = 0.017s$ and an average amplitude of $B_1 = 3.2\mu\text{T}$. The duty cycle was $\text{DC} = 0.98$. The means and precisions (defined as the inverses of the variances) of the prior distributions are shown in table 1.

Furthermore, data sets of multiple Z-spectra with varying saturation powers were simulated for CW and pulsed saturation, since the availability of multiple Z-spectra at different B_1 permits the simultaneous estimation of exchange rate and concentration of CEST pools [7,8,11,29,30]. The average amplitudes were $B_1 = 0.5, 1.0, 2.0, 5.0 \text{ and } 10.0\ \mu\text{T}$. All other parameter values were the same as for the single Z-spectra. The assumed prior distributions are shown in table 1.

Phantom experiments

For continuous-wave saturation experiments a 15mM Iodipamide in phosphate-buffered saline (PBS) solution was measured on a 7T MRI scanner Bruker Avance 300 (Bruker, Ettlingen, Germany), $B_1 = 1.5, 2.0, 3.0 \text{ and } 6.0\ \mu\text{T}$ and $t_p = 5\text{s}$. The pH was adjusted to $\text{pH} = 7.4$ and the temperature to $T = 37°\text{C}$. Frequency offsets were between -10ppm and 10ppm in steps of 0.1ppm. The saturation was followed by a fast spin-echo sequence with centric encoding (repetition time TR/echo time TE/number of excitations NEX/RareFactor =

10s/3.5ms/2/64). T_1 relaxation times were measured using a Rapid Acquisition with Relaxation Enhancement (RARE) sequence with eleven repetition times in the range 50-10000ms. T_1 measurements were performed in a central axial plane with the following parameters: TE/NEX/RareFactor = 11ms/3/2, matrix = 128x128, FOV = 30x30mm^2, slice thickness = 3mm, total acquisition time = 1h 7min. Prior distributions assumed for the Bayesian fit are shown in table 2.

To obtain pulsed saturation data, we measured $12.5, 25.0, 50.0 \text{ and } 100.0 \text{ mM}$ Taurine in water solution which consisted of titrated 0.1% PBS with $\text{pH} = 6.2$ and temperature $T = 23°\text{C}$. The data set was acquired on a 9.4T Agilent MRI scanner using a transmit/receive RF coil with 33mm inner diameter (Rapid Biomedical, Germany). The saturation consisted of 151 Gaussian pulses of duration $t_p = 0.05s$, standard deviation $\sigma_p = 0.017$ and duty cycle of DC = 0.98. The average saturation amplitudes were $\text{B}_1 = 0.78, 1.17, 1.57, 1.96, 2.35, 2.74, 3.13, 3.52, 3.91, 4.31 \text{ μT}$. Each spectrum was sampled at 77 equally spaced frequency offsets between −6ppm and 6ppm. The readout sequence was a single-slice 2D-GRE sequence with a field of view of 20 × 20mm^2, matrix size of 64 × 64, TR = 5s, TE = 1.3ms and slice thickness of 4mm. An Inversion recovery EPI sequence was used to quantify T_1. A global adiabatic inversion pulse (flip angle of 180°, duration 2ms) was applied at the frequency of water followed by 20 equally spaced inversion times from 8.1ms to 7.5s. The other parameters were as follows: $TR = 15$s, $TE = 25.5$ms, slice thickness of 2mm, field of view of 20 × 20mm^2 and matrix size of 64 × 64. For the quantification of T_2 the Carr Purcell Meiboom Gill (CPMG) sequence was used. It consisted of a 90° excitation pulse (sinc pulse of 2ms duration) in x-direction followed by 15 refocusing pulses in y-direction (flip angle of 180°, sinc shape and duration of 1.6ms). The

other parameters were: TR = 3s, τ_{CPMG} = 8.33ms, slice thickness of 2mm, field of view of 20 × 20mm^2 and matrix size of 64 × 64.

For each phantom, mean Z-spectra at various saturation powers were obtained by averaging the measured intensities in a circular region of interest (ROI) covering the phantom vials' cross sections. Additionally, pixel-wise fits were performed on the Taurine data. The Z-spectra were normalized by the average signal of the 5 most negative frequency offsets in order to reduce the impact of noise.

For the implementation of the fitting algorithm the Variational Bayesian (VB) algorithm available in the FMRIB Software Library (v5.0) was used. We extended the model library by replacing the full BM model by the simplified models described by equations 3 and 5. Fits were also performed with the full BM model (according to [11]) to compare the accuracy of parameter estimates and processing times between the two models.

4. Results

The simulated Z-spectra and fits obtained with the modified algorithm are shown in figure 1. The individual Z-spectra simulated for a single B_1 (figure 1a and 1b) are well described by the fitted spectrum. The standard deviation of the fit residuals was $\sigma_{res} = 0.019$ for CW and $\sigma_{res} = 0.029$ for pulsed saturation. The ground truth parameter values are included in the σ-credible intervals of the posterior distributions of k_{ba} and T_{2b} (table 1). In comparison, fitting the BM equations numerically also led to matching parameter estimates.

Z-spectra simulated at multiple B_1 values (figure 1c and d) are also well described by the fitted model ($\sigma_{res} = 0.02$), though larger residuals are observable at higher B_1 ($\sigma_{res} = 0.05$), especially close to on-resonance. The ground truth values agreed with the estimates resulting from the fit of the CW saturation as well as the pulsed saturation data (table 1). Fitting the BM equations numerically led to matching estimates in the case of CW saturation, however, the numerical fit of pulsed saturation data yielded estimates that diverged significantly from the ground truth.

Large differences in processing times between analytical and numerical algorithm were observed. For CW saturation, the algorithm based on the simplified analytical forward model was 51 times faster than the numerical forward model when a single B_1 Z-spectrum was fitted and 48 times faster for the fitting of multiple B_1 Z-spectra. For pulsed saturation, the analytical solution led to a 127-fold decrease in processing time for the single Z-spectrum data set and a 108-fold decrease for the multiple B_1 Z-spectra data set.

The CW saturation Z-spectra of Iodipamide and the corresponding fits obtained with analytical and numerical models are shown in figure 2. The fits were obtained with a fixed relaxation time $T_{1a} = 3.3$s as determined by the Inversion Recovery sequence. The estimated probability distributions for M_{0b}, k_{ba}, ω_b, $\omega_a$and T_{2a} are shown in table 2. Both algorithms led to matching estimates for M_{0b}, k_{ba} and ω_b, but $\Delta\omega_{0,off}$ and T_{2a} are significantly different.

The averaged Z-spectra of the Taurine phantoms and the corresponding fits are shown in figure 3. The modelled Z-spectra describe the measured data reasonably well and residuals are negligible, except close to on resonance and at small concentrations. Assuming a fixed relaxation time $T_{1a} = 3.2$s, the fit based on the simplified analytical equations yielded the parameter estimates for Taurine concentrations of 12.5, 25.0, 50.0, 100.0mM shown in table 3.

The resulting parameter maps of pixel-wise fits of the Taurine Z-spectra are shown in figure 4. For M_{0a}, M_{0b}, k_{ba}, $\omega_{0,off}$ and $\omega_b$we obtained smooth parameter maps in each phantom, except from a few pixels at the edges of the plastic tubes. In accordance with the fit results of the averaged Z-spectra, k_{ba} and M_{0b} increase with the Taurine concentration. The T_{2a} map is smooth only for the low concentration phantom, but more erroneous estimates were observed the higher the concentration.

5. Discussion

In this study, a Variational Bayesian algorithm for fast Bayesian inference [13] has been applied to fit CEST data. In contrast to a previous approach based on a general solution of the BM equations [11], we used simplified analytical models with the aim to reduce processing time. To assess the processing times as well as the convergence and accuracy of this evaluation, the algorithm was applied to Z-spectra obtained from simulations as well as phantom experiments under both CW and pulsed saturation. The results show that the simplified algorithm converges to a solution that describes the data well and which allows to

estimate parameters with an accuracy and precision that is comparable with the previous algorithm.

With this approach, it was however possible to considerably reduce processing time. The approximately 50-fold reduction of computational time for CW saturation can largely be attributed to the reduced complexity of the applied analytical solution. In more details, the numerical solution requires the relatively time-consuming calculation of a matrix exponential, whereas equation 3 comprises only basic arithmetic operations. As the Variational Bayesian algorithm iteratively updates the parameter estimates until convergence, the respective solutions are evaluated for each update.

In the case of pulsed saturation, the reduction of processing time was greater (up to 127-fold), although the analytical formula for pulsed saturation (equation 5) is more complex than the analytical formula for CW saturation. This great reduction is possible because the numerical solution requires a separation of the pulse shape into multiple intervals with approximately constant amplitude, each of which requires the numerical evaluation of equation 5. In contrast, with the simplified model the averaging of $R_{1\rho}$ over the pulse shape makes it possible to obtain the parameter update for each iteration with only one evaluation of equation 5.

Assuming the processing times observed in the simulated experiments, the time required for fitting a single slice of 100×100 pixels is reduced from 5.6 hours to 6.5 minutes in the case of continuous-wave saturation. Fitting a slice of these dimensions with pulsed saturation would be infeasible with the numerical solution (~44 days) and would take 8.3

hours with the analytical approximation. Such improvements in processing time might be crucial when quantitative CEST methods are considered for clinical routine. Note that we would expect such processing times to be further reduced using implementations on computer graphics cards.

The accuracy of the fit results was comparable to the accuracy obtained with the previous algorithm [11]. In the simulation study the observed residuals (~2%) for CW saturation Z-spectra fits were dominated by the added Gaussian noise. For pulsed saturation, larger residuals (<5%) were observed, which can be attributed to the assumptions made by the analytical model. Particularly the application of effective parameters, averaged over the pulse shape, and the choice of the heuristic value α_{start} are likely to cause the observed deviations.

Only relatively small deviations were observed between the means of the posterior distributions and the ground truth (< 4% for k_{ba} and T_{2b}). As these deviations fall within the σ-credible intervals of the estimated posterior distributions, they are likely due to the influence of noise. This is supported by the deviations resulting from the numerical algorithm, which are of similar magnitude.

When the solute concentration was additionally set as a free parameter for the simultaneous fitting of multiple Z-spectra at varying B_1, the numerical solution led to wrong parameter estimates for the pulsed saturation data. It can be assumed that the algorithm converged to a locally optimal solution, rather than the global optimum. Providing more specific prior information about expected parameters could help to avoid this behaviour.

For the multiple B_1 Z-spectra fits, the deviation between ground truth and the means of the posterior distributions increased to up to 10% for CW saturation and up to 20% for pulsed saturation, however these increases were captured within the σ-credible intervals, whose larger width can be attributed to the degree of correlation between solute concentration and exchange rate that has been reported in other studies [31].

In order to fit the Iodipamide Z-spectrum, 6 model parameters were estimated by the analytical and numerical algorithms (table 2). The comparison shows deviations of the posterior distribution which are included in the σ-credible intervals and are therefore not significant for M_{0b}, k_{ba} and ω_b. On the other hand, the differences of $\Delta\omega_{0,off}$ (≈0.014ppm) and T_{2a} (≈ 22ms) don't fall within the credible intervals. As discussed in regard to the deviations in the simulated study, these discrepancies can be explained either by convergence issues (local optima) or by the limited range of validity of the assumptions of the analytical model. The latter is less likely, since equations 3-13 were shown to be in good agreement with the numerical solution of the BM equations in [24] for the parameters estimated here. The increased asymmetry of the residuals with respect to the water peak in the numerical solution (figure 2b) suggests that the B_0 correction by estimating $\Delta\omega_{0,off}$ was not successful, resulting in a local optimum and the observed significant biases in $\Delta\omega_{0,off}$ and T_{2a}.

The determined relative Iodipamide equilibrium magnetizations (M_{0b}, = 2.6(3)·10^{-4} and M_{0b}, = 2.9(4)·10^{-4} for analytical and numerical solutions respectively) are in agreement with the expected value of a 15mM solution, assuming that both Iodipamide and water molecules have 2 exchanging proton sites ($M_{0b} = \frac{15mM \cdot 2protons}{55M \cdot 2protons} \approx 2.7 \cdot 10^{-4}$).

The transverse relaxation time of Iodipamide T_{2b} was determined with large uncertainty by both, numerical and analytical algorithm. This is due to the small influence of T_{2b} on the shape of the Z-spectrum.

The increased magnitude of residuals close to the water peak was also observed in the simulation experiments and can be attributed to the breakdown of the model assumption of negligible rotation of the water magnetization about the effective magnetic field. This effect becomes more important for shorter pulse duration t_p, higher B_1 and longer T_{2a}.

Furthermore, it is also possible that the fixed value for T_{1a} deviates sufficiently from its true value to contribute to the larger residuals at the water peak.

The Z-spectra of Taurine solutions of different concentrations were acquired with pulsed saturation. As expected, a linear relation was measured between the Taurine concentration and M_{0b} (figure 5a). Furthermore, a linear relation was found between exchange rate and concentration (figure 5b), which is in line with recently reported previous measurements based on non-Bayesian fits [32].

The estimates of T_{2a} show small differences of the transverse relaxation time of water between the phantoms and larger credible intervals at higher concentration. The increased credible intervals can be explained by a stronger correlation between k_{ba} and T_{2a} at higher concentrations, as both parameters influence the width of the water peak in a similar way. At large exchange rates, as observed in the phantoms with high Taurine concentration, k_{ba} dominates the width of the water peak and makes the estimation of T_{2a} more difficult. On the other hand, when k_{ba} is small, the width of the water peak is dominated by T_{2a}, which can therefore be estimated more accurately.

The influence of T_{2b} on the Z-spectra is negligible under the chosen experimental settings, which means that an accurate estimation of this parameter is not possible.
The parameter maps of M_{0a} , M_{0b}, k_{ba} and ω_b (figure 4 a-d) agree with the fit results obtained from the fit of the averaged Z-spectra. The map of $\Delta\omega_{0,off}$ corresponds to the measured B_0 map and reveals inhomogeneities of up to ± 0.15ppm. In this way, an additional acquisition of a B_0 map and pre-processing of the Z-spectra can be avoided. The T_{2a} map confirms the interpretation that a large exchange rate reduces the accuracy of the T_{2a} estimation, leading to unrealistic parameter estimates of more than 4s for many pixels.

To date, the Variational Bayesian algorithm on which this study is based [13] is the only Bayesian algorithm incorporating the BM equations that has been applied to fit Z-spectra. The main limitation of the proposed method compared to the previous implementation originates from the assumptions of the employed analytical solution, which is valid only for slow and intermediate exchange regimes. While the agents chosen in this study fulfil this requirement, other agents, especially at high pH, might yield very different estimates when fitted with either the analytical or the numerical solution, due to violation of the assumptions made when deriving the analytical solutions. Furthermore, the analytical solutions employed in this study were developed for a two-pool model and need to be extended to three or more pools to be applicable to *in vivo* data. However, other analytical solutions exist for different exchange regimes and multiple pools [18–23,33] and/or may be developed in the future that can be combined with Bayesian model-fitting approaches to reduce processing times. Problems related to the correlation between model parameters such as agent concentration and exchange rate are not mitigated by employing improved analytical solutions, as the correlation stems from the data acquisition itself. Instead,

improving the sampling strategy can lead to a smaller degree of correlation in the data. An improved sampling strategy might also be advantageous to reduce the measurement time [34]. Sampling the full Z-spectrum might not be feasible in a clinical setting, especially when 3D images are desired.

6. Conclusion

A Bayesian fitting algorithm based on approximate analytical solutions of the BM equations has been employed to fit Z-spectra. A considerable reduction of processing times was observed, while the accuracy of estimated parameters was maintained in simulated and phantom experiments. The application of other analytical solutions might further improve the performance of the algorithm.

7. Acknowledgements

We would like to thank Prof. Dr. M. A. Chappell for providing Matlab scripts to navigate the Variational Bayesian (VB) algorithm for CEST of the FMRIB Software Library.

Appendix A

For small population fractions ($f_b = \frac{M_{0b}}{M_{0a}} \ll 1$), the parameter $R_{1\rho}$ can be regarded as the rate which is perturbed by chemical exchange expressed by the exchange-dependent relaxation rate R_{ex}:

$$R_{1\rho} = R_{eff} + R_{ex}, \tag{11}$$

where R_{eff} is the unperturbed relaxation rate in the rotating frame, i.e. without exchange, which can be approximated by [35]:

$$R_{eff} = \cos^2(\theta)\, R_{1a} + \sin^2(\theta)\, R_{2a}. \tag{12}$$

The following assumptions are made to obtain a simplified expression for R_{ex}:

1. The influence of R_{1a} and R_{2a} on R_{ex} is negligible,
2. $R_{1b} \ll R_{1a}$ and $R_{1b} \ll k_{ba}$,
3. R_{ex} can be linearized in k_{ab}.

Under these assumptions, R_{ex} can be approximated by:

$$R_{ex} = \frac{R_{ex}^{max} \frac{\Gamma^2}{4}}{\frac{\Gamma^2}{4} + \Delta\omega_b^2} \tag{13}$$

with

$$R_{ex}^{max} = f_b k_{ba} \sin^2(\theta) \frac{(\omega_b - \omega_a)^2 + \frac{R_{2b}}{k_{ba}}(\omega_1^2 + \Delta\omega^2) + R_{2b}(k_{ba} + R_{2b})}{\frac{\Gamma^2}{4}} \tag{14}$$

and

$$\Gamma = 2\sqrt{\frac{k_{ba}+R_{2b}}{k_{ba}}\omega_1^2 + (k_{ba} + R_{2b})^2}. \tag{15}$$

Here, $\Delta\omega_b = \omega_{rf} - \omega_b$ is the difference between the frequency of the CW irradiation and the resonance frequency of pool b.

Appendix B

Expressions for d_{aa} and d_{ab} were presented in [22], as part of the biexponential solution of the BM equations for $B_1 = 0$ (no saturation) and negligible transverse magnetization ($M_{ix} = M_{iy} = 0$):

$$d_{aa} = \frac{(\lambda_1 + R_{1b} + k_{ba})\exp(\lambda_1 t_d) - (\lambda_2 + R_{1b} + k_{ba})\exp(\lambda_2 t_d)}{\lambda_1 - \lambda_2} \quad (16)$$

$$d_{ab} = \frac{k_b(\exp(\lambda_1 t_d) - \exp(\lambda_2 t_d)}{\lambda_1 - \lambda_2} \quad (17)$$

Expressions for λ_1 and λ_2 are:

$$\lambda_1 = -\frac{1}{2}(k_a + k_b + R_{1a} + R_{1b} + \sqrt{(k_a + k_b + R_{1a} + R_{1b})^2 - 4(k_b R_{1a} + k_a R_{1b} + R_{1a} R_{1b})} \quad (18)$$

$$\lambda_2 = -\frac{1}{2}(k_a + k_b + R_{1a} + R_{1b} - \sqrt{(k_a + k_b + R_{1a} + R_{1b})^2 - 4(k_b R_{1a} + k_a R_{1b} + R_{1a} R_{1b})} \quad (19)$$

Appendix C

Figure 6 shows the dependence of α_{start} based on the exchange rate k_{ba} and the average pulse amplitude B_1. For large k_{ba} it is obvious that α_{start} approaches 1, whereas α_{start} approaches 0 for small k_b. In the intermediate regime of amide exchange rates, a value of $\alpha_{start} \approx 0.5$ is a reasonable choice. In figure 7 the effect of this choice of α_{start} on the analytical solution is shown for different saturation powers and assuming an exchange rate of $k_{ba} = 30$Hz. Note that the analytical solution is closer to the numerical solution for $\alpha_{start} = 0.5$ than for $\alpha_{start} = 0$ or $\alpha_{start} = 1$. For faster exchange rates the influence of α_{start} on the Z-spectrum is negligible (Figure 8). Hence, $\alpha_{start} = 0.5$ was chosen for all fits in this study.

8. References

1. Ward K., Aletras A., Balaban R. A New Class of Contrast Agents for MRI Based on Proton

Chemical Exchange Dependent Saturation Transfer (CEST). Journal of Magnetic Resonance. 2000;143(1):79–87. doi:10.1006/jmre.1999.1956

2. Van Zijl PCM, Yadav NN. Chemical exchange saturation transfer (CEST): What is in a name and what isn't? Magnetic Resonance in Medicine. 2011;65(4):927–948. doi:10.1002/mrm.22761

3. Longo DL, Cutrin JC, Michelotti F, Irrera P, Aime S. Noninvasive evaluation of renal pH homeostasis after ischemia reperfusion injury by CEST-MRI. NMR in Biomedicine. 2017;30(7):e3720. doi:10.1002/nbm.3720

4. Longo DL, Bartoli A, Consolino L, Bardini P, Arena F, Schwaiger M, Aime S. In vivo imaging of tumor metabolism and acidosis by combining PET and MRI-CEST pH imaging. Cancer Research. 2016;76(22):6463–6470. doi:10.1158/0008-5472.CAN-16-0825

5. Tietze A, Blicher J, Mikkelsen IK, Østergaard L, Strother MK, Smith SA, Donahue MJ. Assessment of ischemic penumbra in patients with hyperacute stroke using amide proton transfer (APT) chemical exchange saturation transfer (CEST) MRI. NMR in Biomedicine. 2014;27(2):163–174. doi:10.1002/nbm.3048

6. Sun PZ, Wang Y, Dai ZZ, Xiao G, Wu R. Quantitative chemical exchange saturation transfer (qCEST) MRI - RF spillover effect-corrected omega plot for simultaneous determination of labile proton fraction ratio and exchange rate. Contrast Media and Molecular Imaging. 2014;9(4):268–275. doi:10.1002/cmmi.1569

7. Dixon WT, Ren J, Lubag AJM, Ratnakar J, Vinogradov E, Hancu I, Lenkinski RE, Sherry AD. A concentration-independent method to measure exchange rates in PARACEST agents. Magnetic Resonance in Medicine. 2010;63(3):625–632. doi:10.1002/mrm.22242

8. Mcmahon MT, Gilad AA, Zhou J, Sun PZ, Bulte JWM, Zijl PCM Van. Quantifying Exchange Rates in Chemical Exchange Saturation Transfer Agents Using the Saturation Time and

Saturation Power Dependencies of the Magnetization Transfer Effect on the Magnetic Resonance Imaging Signal (QUEST and QUESP): pH Calibration for Poly. Magn Reson Med. 2006;55(4):836–847. doi:10.1126/scisignal.2001449.Engineering

9. Sun PZ. Simplified quantification of labile proton concentration-weighted chemical exchange rate (k ws) with RF saturation time dependent ratiometric analysis (QUESTRA): Normalization of relaxation and RF irradiation spillover effects for improved quantitative ch. Magnetic Resonance in Medicine. 2012;67(4):936–942. doi:10.1002/mrm.23068

10. Jones CK, Huang A, Xu J, Edden RAE, Schär M, Hua J, Oskolkov N, Zacà D, Zhou J, McMahon MT, et al. Nuclear Overhauser enhancement (NOE) imaging in the human brain at 7T. NeuroImage. 2013;77:114–124. doi:10.1016/j.neuroimage.2013.03.047

11. Chappell MA, Donahue MJ, Tee YK, Khrapitchev AA, Sibson NR, Jezzard P, Payne SJ. Quantitative Bayesian model-based analysis of amide proton transfer MRI. Magnetic Resonance in Medicine. 2013;70(2):556–567. doi:10.1002/mrm.24474

12. Ray KJ, Larkin JR, Tee YK, Khrapitchev AA, Karunanithy G, Barber M, Baldwin AJ, Chappell MA, Sibson NR. Determination of an optimally sensitive and specific chemical exchange saturation transfer MRI quantification metric in relevant biological phantoms. NMR in Biomedicine. 2016;29(11):1624–1633. doi:10.1002/nbm.3614

13. Chappell MA, Groves AR, Whitcher B, Woolrich MW. Variational Bayesian inference for a nonlinear forward model. IEEE Transactions on Signal Processing. 2009;57(1):223–236. doi:10.1109/TSP.2008.2005752

14. Woessner DE, Zhang S, Merritt ME, Sherry AD. Numerical solution of the Bloch equations provides insights into the optimum design of PARACEST agents for MRI. Magnetic Resonance in Medicine. 2005;53(4):790–799. doi:10.1002/mrm.20408

15. Murase K, Tanki N. Numerical solutions to the time-dependent Bloch equations

revisited. Magnetic Resonance Imaging. 2011;29(1):126–131. doi:10.1016/j.mri.2010.07.003

16. Bloch F. Nuclear induction. Physical Review. 1946;70(7–8):460–474. doi:10.1103/PhysRev.70.460

17. McConnell HM. Reaction Rates by Nuclear Magnetic Resonance. The Journal of Chemical Physics. 1958;28(3):430–431. doi:10.1063/1.1744152

18. Zhou J, Zijl PCM van. Chemical exchange saturation transfer imaging and spectroscopy. Progress in Nuclear Magnetic Resonance Spectroscopy. 2006;48(2–3):109–136. doi:10.1016/j.pnmrs.2006.01.001

19. McMahon MT, Gilad AA, Zhou J, Sun PZ, Bulte JWM, Van Zijl PCM. Quantifying exchange rates in chemical exchange saturation transfer agents using the saturation time and saturation power dependencies of the magnetization transfer effect on the magnetic resonance imaging signal (QUEST and QUESP): pH calibration for poly. Magnetic Resonance in Medicine. 2006;55(4):836–847. doi:10.1002/mrm.20818

20. Sun PZ, Murata Y, Lu J, Wang X, Lo EH, Sorensen AG. Relaxation-compensated fast multislice amide proton transfer (APT) imaging of acute ischemic stroke. Magnetic Resonance in Medicine. 2008;59(5):1175–1182. doi:10.1002/mrm.21591

21. Zaiss M, Bachert P. Chemical exchange saturation transfer (CEST) and MR Z-spectroscopy in vivo: a review of theoretical approaches and methods. Phys. Med. Biol. 2013;58:221–269. doi:10.1088/0031-9155/58/22/R221

22. Roeloffs V, Meyer C, Bachert P, Zaiss M. Towards quantification of pulsed spinlock and CEST at clinical MR scanners : an analytical interleaved saturation – relaxation (ISAR) approach. NMR in Biomedicine. 2015;28(October 2014):40–53. doi:10.1002/nbm.3192

23. Gochberg DF, Does MD, Zu Z, Lankford CL. Towards an analytic solution for pulsed CEST. NMR in Biomedicine. 2018 May;31(5):e3903. doi:10.1002/nbm.3903

24. Zaiss M, Bachert P. Exchange-dependent relaxation in the rotating frame for slow and intermediate exchange - modeling off-resonant spin-lock and chemical exchange saturation transfer. NMR in Biomedicine. 2013;26(5):507–518. doi:10.1002/nbm.2887

25. Roell SA, Dreher W, Leibfritz D. A general solution of the standard magnetization transfer model. Journal of Magnetic Resonance. 1998;132(1):96–101. doi:10.1006/JMRE.1998.1393

26. Michaeli S, Sorce DJ, Springer CS, Ugurbil K, Garwood M. T1ρMRI contrast in the human brain: Modulation of the longitudinal rotating frame relaxation shutter-speed during an adiabatic RF pulse. Journal of Magnetic Resonance. 2006;181(1):135–147. doi:10.1016/j.jmr.2006.04.002

27. Mangia S, Liimatainen T, Garwood M, Michaeli S. Rotating frame relaxation during adiabatic pulses vs. conventional spin lock: simulations and experimental results at 4 T. Magnetic Resonance Imaging. 2009;27(8):1074–1087. doi:10.1016/j.mri.2009.05.023

28. Zu Z, Janve VA, Xu J, Does MD, Gore JC, Gochberg DF. A new method for detecting exchanging amide protons using chemical exchange rotation transfer. Magnetic Resonance in Medicine. 2013;69(3):637–647. doi:10.1002/mrm.24284

29. Desmond KL, Stanisz GJ. Understanding quantitative pulsed CEST in the presence of MT. Magnetic Resonance in Medicine. 2012;67(4):979–990. doi:10.1002/mrm.23074

30. Sun PZ. Simultaneous determination of labile proton concentration and exchange rate utilizing optimal RF power: Radio frequency power (RFP) dependence of chemical exchange saturation transfer (CEST) MRI. Journal of magnetic resonance (San Diego, Calif. : 1997). 2010;202(2):155–61. doi:10.1016/j.jmr.2009.10.012

31. Xu J, Zaiss M, Zu Z, Li H, Xie J, Gochberg DF, Bachert P, Gore JC. On the origins of chemical exchange saturation transfer (CEST) contrast in tumors at 9.4T. NMR in

Biomedicine. 2014;27(4):406–416. doi:10.1002/nbm.3075

32. Demetriou E, Tachrount M, Zaiss M, Shmueli K, Golay X. PRO-QUEST: An effective and rapid method for exchange rate quantification based on PROgressive saturation for Quantifying Exchange using Saturation Times in Chemical Exchange Saturation Transfer (CEST). 2017.

33. Davis DG, Perlman ME, London RE. Direct Measurements of the Dissociation-Rate Constant for Inhibitor-Enzyme Complexes via the T1ρand T2(CPMG) Methods. Journal of Magnetic Resonance, Series B. 1994;104(3):266–275. doi:10.1006/jmrb.1994.1084

34. Tee YK, Khrapitchev AA, Sibson NR, Payne SJ, Chappell MA. Optimal sampling schedule for chemical exchange saturation transfer. Magnetic Resonance in Medicine. 2013;70(5):1251–1262. doi:10.1002/mrm.24567

35. Trott O, Palmer AG. Theoretical study of R1(rho) rotating-frame and R2 free-precession relaxation in the presence of n-site chemical exchange. Journal of Magnetic Resonance. 2004;170(1):104–112. doi:10.1016/j.jmr.2004.06.005

Figure 1: Fit results of simulated data sets obtained with the simplified analytical equations for a two-pool model of an amide in water solution: single B_1 continuous-wave saturation (a), single B_1 pulsed saturation (b), multiple B_1 continuous-wave saturation (c) and multiple B_1 pulsed saturation (d). The single B_1 Z-spectra were simulated with an average amplitude of $B_1 = 3.2\mu T$. For multiple B_1 Z-spectra we employed $B_1 = 0.5, 1.0, 2.0, 5.0$ and 10.0 µT.

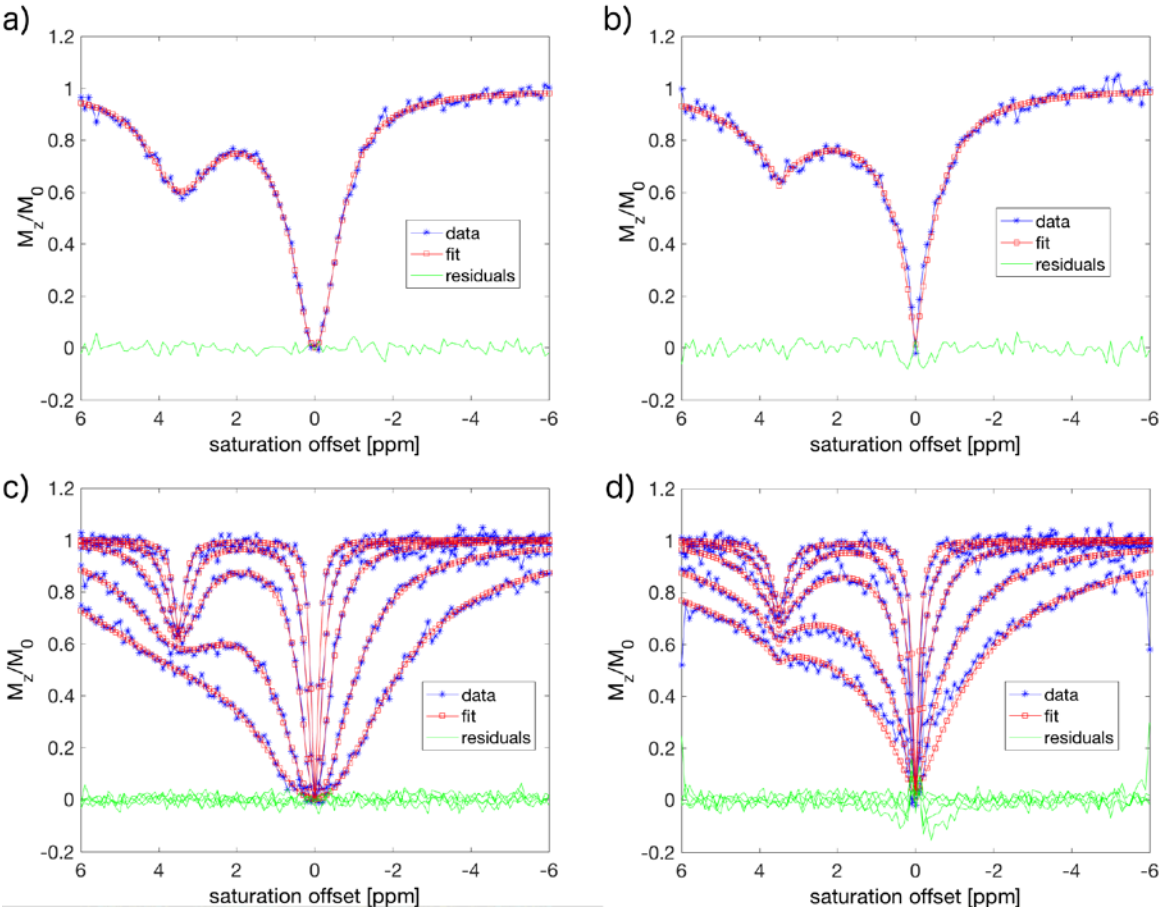

Figure 2: Z-spectra of a 15mM Iodipamide in PBS solution at pH = 7.4 and T = 37˚C. The fit was obtained with the simplified analytical equations (a) and the numerical model (b).

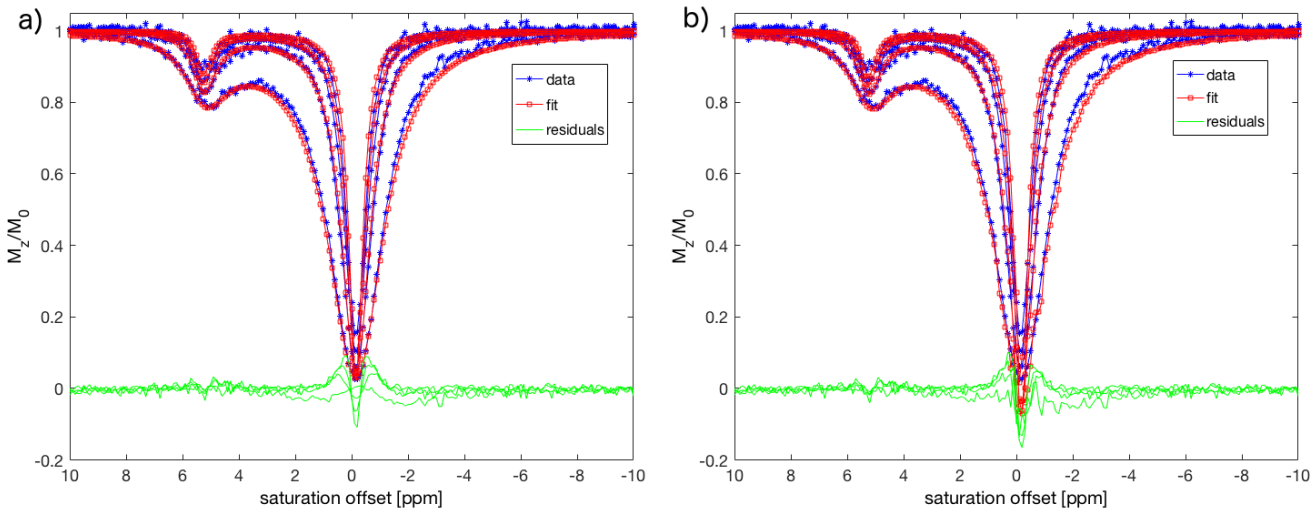

Figure 3: Z-spectra of 12.5mM (a), 25.0mM (b), 50.0mM (c), 100.0mM(d) Taurine in PBS solutions at pH = 6.2 and T = 23˚C. The saturation pulse average amplitude was varied with $B_1 = 0.78, 1.17, 1.57, 1.96, 2.35, 2.74, 3.13, 3.52, 3.91, 4.31$ μT. The fits were obtained with the simplified analytical equations for a two-pool model.

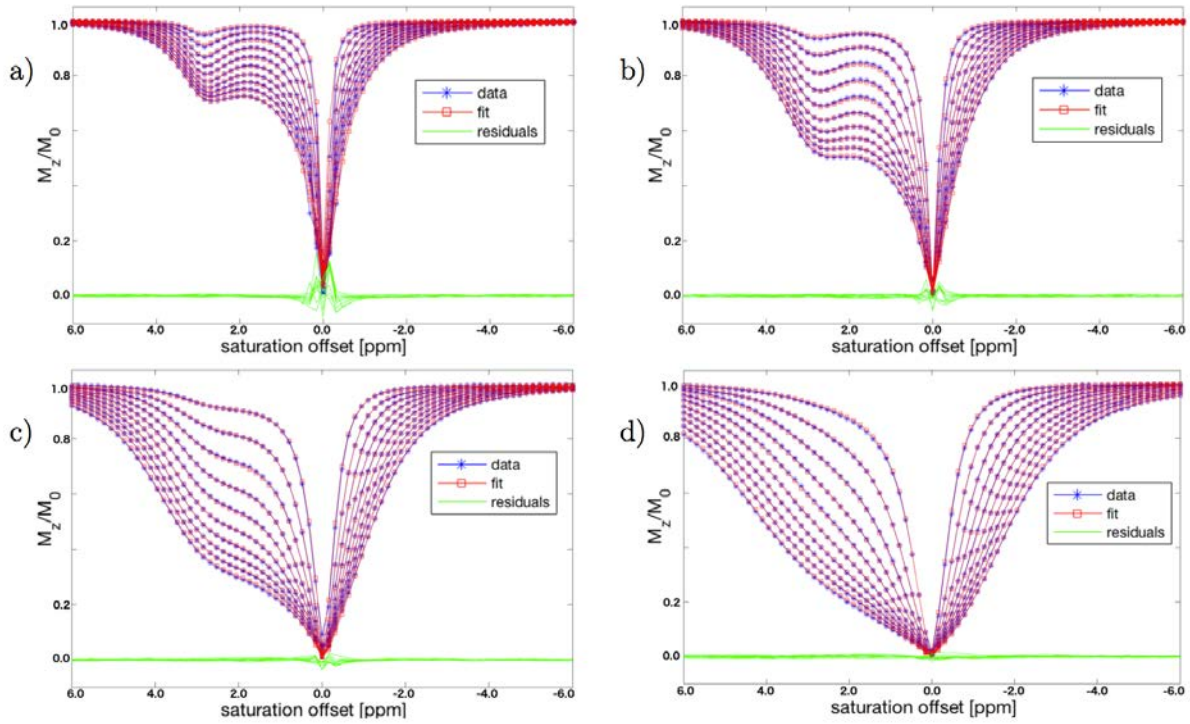

Figure 4: Parameter maps obtained from pixel-wise Bayesian fits of Z-spectra at multiple B_1 of Taurine in PBS solutions at pH = 6.2 and T=23˚C a) M_{0a}, b) M_{0b}, c) k_{ba} in Hz, d) $\omega_{0,off}$ in ppm, e) ω_b in ppm, f) T_{2a} in s. The Taurine concentrations from the bottom tube to the top tube are: 12.5mM, 25.0mM, 50.0mM, 100.0mM. The maps were masked to include only those pixels showing the Taurine phantom vials.

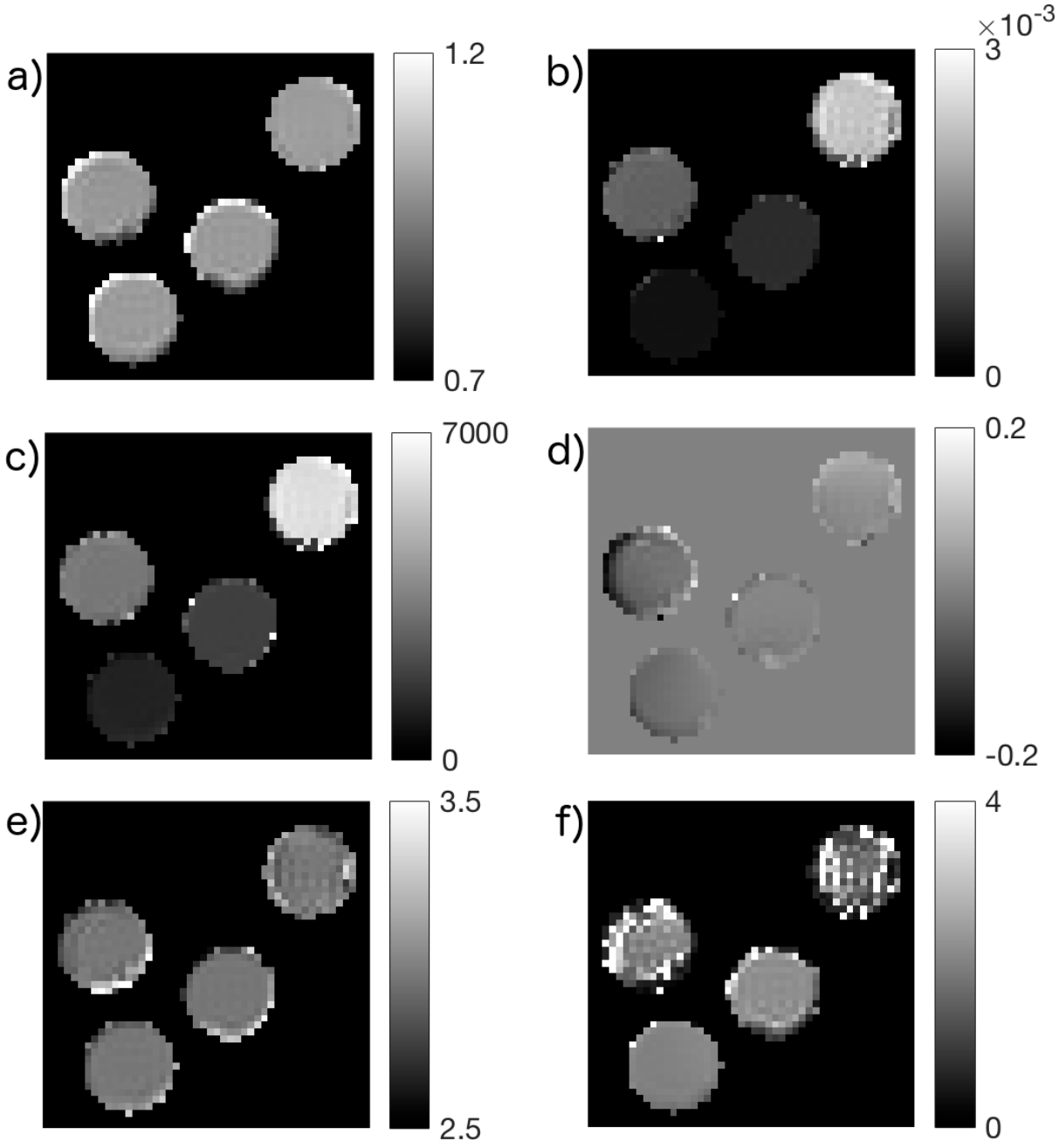

Figure 5: The figures show the linear dependencies between Taurine concentration and the means of the distributions of the equilibrium magnetization of the Taurine pool M_{0b} (a) and the exchange rate k_{ba} (b), respectively as estimated by the fit. The error bars correspond to the σ-credible intervals. The linear regression lines are weighted least squares lines where the weights are inverse variances of the estimated parameter distributions.

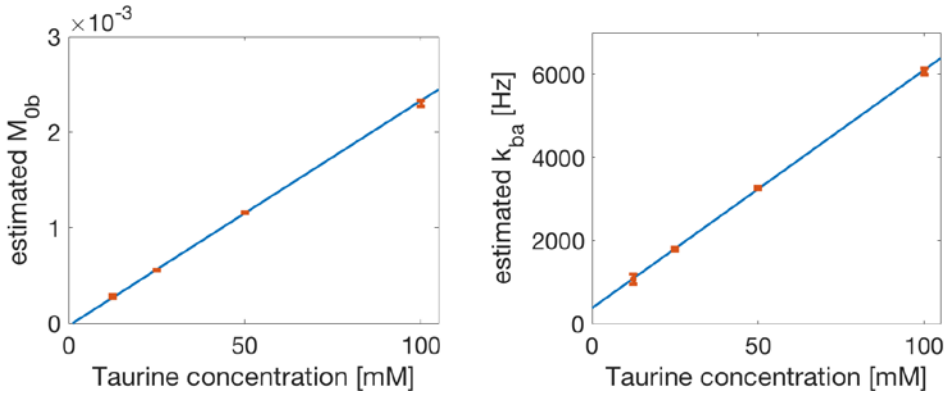

Figure 6: Dependence of the ideal value of α_{start} on the exchange rate and the average saturation amplitude. The value was calculated according to $\alpha_{start} = \frac{\Psi_{max}-\Psi}{\Psi_{max}-\Psi_{\min}}$, where $\Psi = \frac{M_{zb}(t=t_p)}{M_{za}(t=t_p)}$ was calculated by solving the 2-pool BM equations numerically. The simulation parameters were the same as those of the simulation experiment described in the Methods chapter.

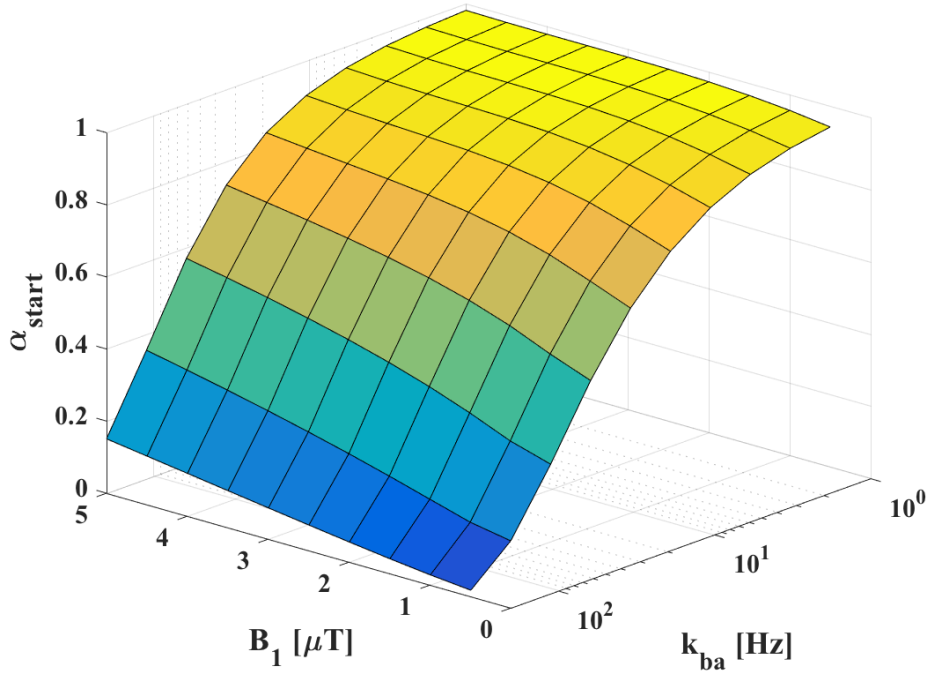

Figure 7: Comparison of the effect of different values of α_{start} on the analytical solution for pulsed saturation with Gaussian pulses at different average saturation amplitudes. The left column shows full Z-spectra and the right column shows a magnification of the solute peak. The simulation parameters were the same as those of the simulation experiment described in the Methods chapter, in particular $k_{ba} =$ 30Hz. At this exchange rate, $\alpha_{start} = 0.5$ is a reasonable choice.

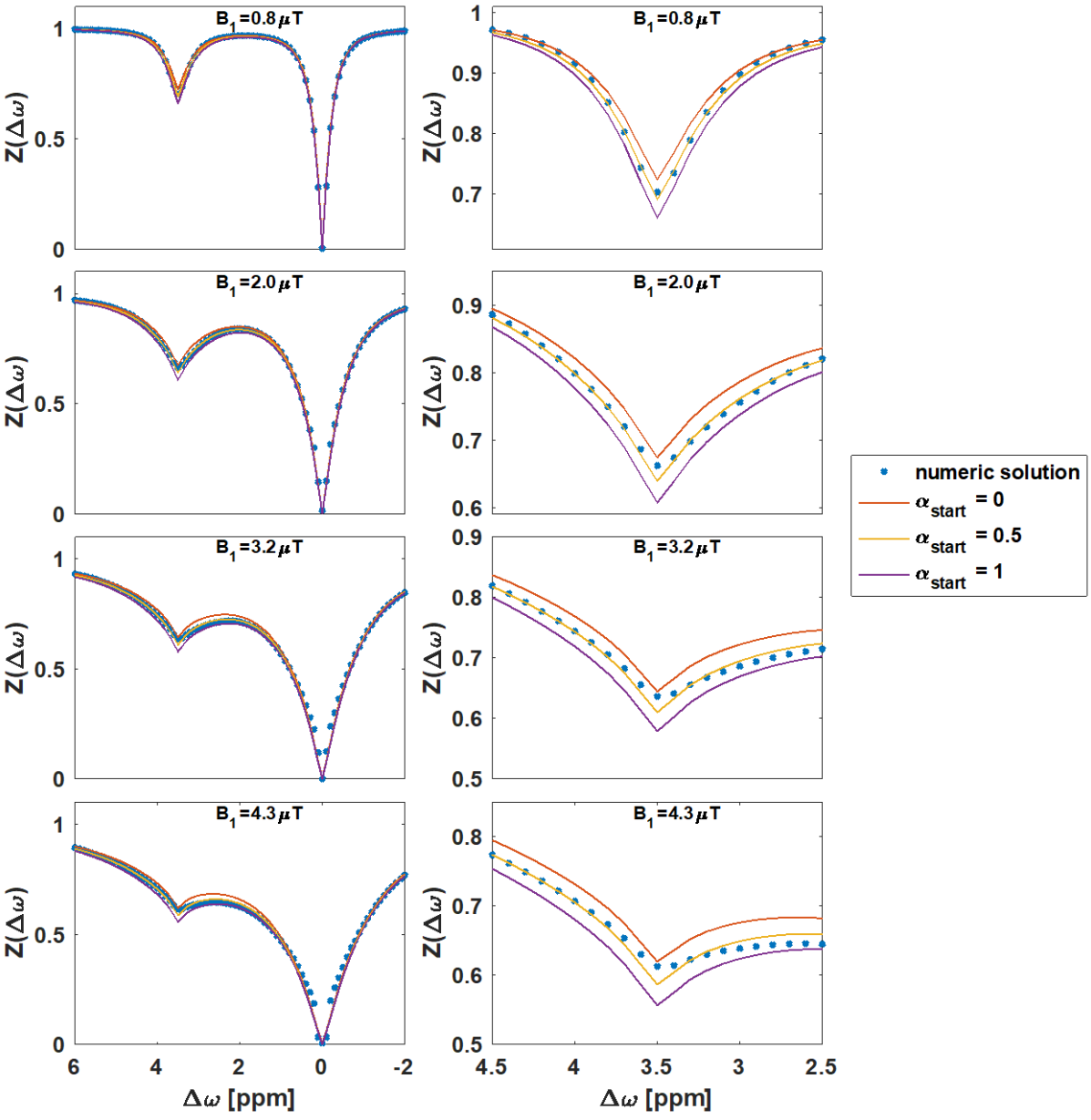

Figure 8: Comparison of the effect of different values of α_{start} on the analytical solution for pulsed saturation with Gaussian pulses at different average saturation amplitudes. Regarding the simulation parameters, the only difference to Figure 7 is the exchange rate which was increased to $k_{ba} = 300\text{Hz}$. The figure shows that at faster exchange rates, the influence of α_{start} on the analytical Z-spectrum is negligible. Note, that the analytical Z-spectra overlap and are therefore almost not distinguishable.

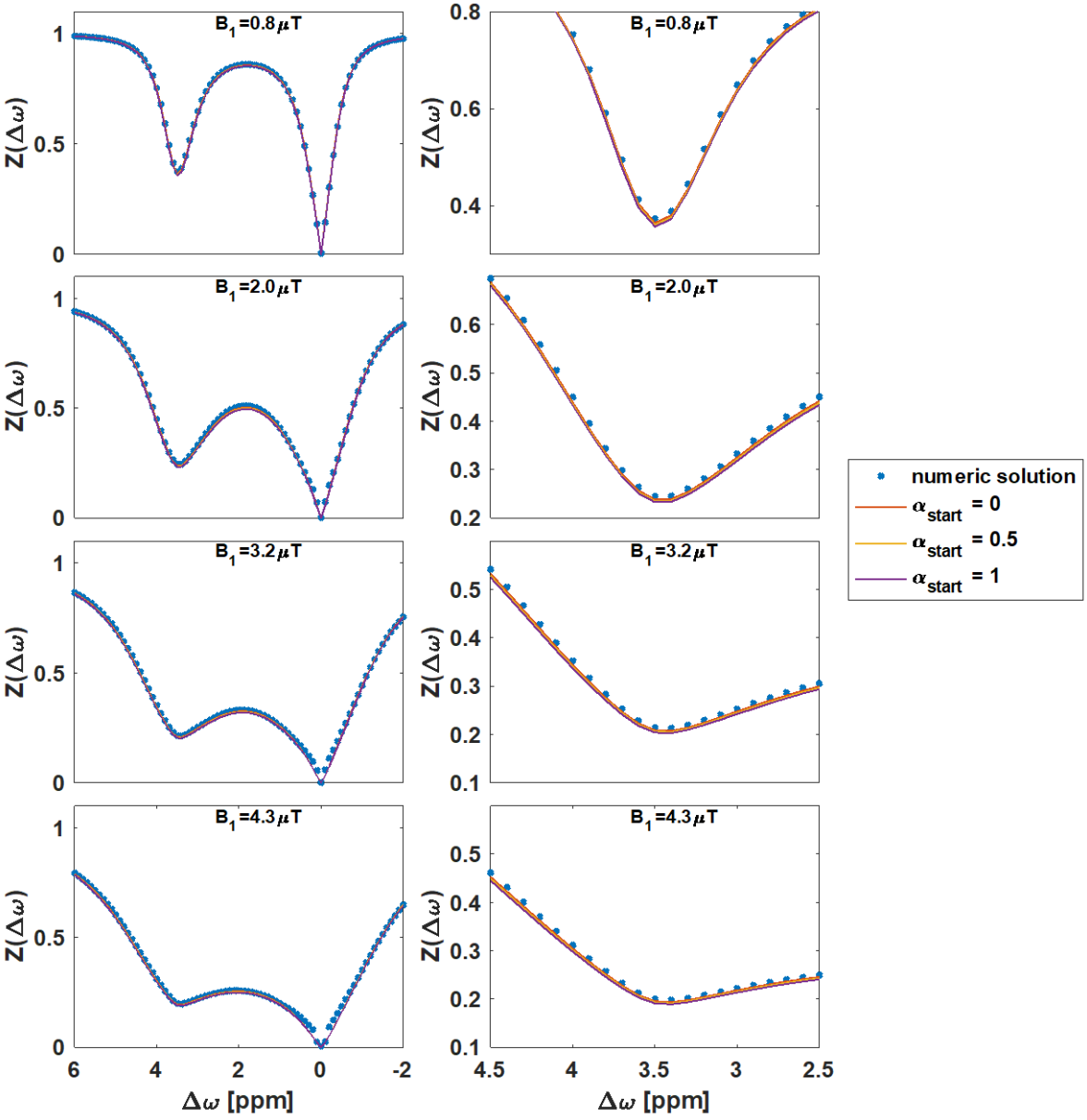

Table 1: Comparison between the ground truth of the BM simulations and the parameter estimates returned by the Bayesian algorithm with the numerical and the analytical models. The uncertainty in brackets indicates the standard deviation of the Gaussian posterior distribution and refers to the last digits of the mean, e.g. $0.0157(14) = 0.0157 \pm 0.0014$. The processing times were measured on a 2.9GHz Intel Core i5 processor.

		prior		CW saturation		pulsed saturation	
parameter	truth	mean	prec.	analytical	numerical	analytical	numerical
single B1							
k_{ba}[Hz]	30	90	10^{-12}	29.2(8)	29.4(8)	29.6(1.3)	30.4(1.2)
T_{2b}[s]	0.015	0.005	10^{-12}	0.0157(14)	0.0149(13)	0.0144(22)	0.0156(20)
proc. time [s]	-	-	-	0.039	2	3	382
multi B1							
M_{0b}	0.007	0.01	10^{-12}	0.0076(20)	0.0076(17)	0.0067(19)	0.0227(47)
k_{ba}[Hz]	30	90	10^{-12}	27.2(7.2)	27.3(6.0)	30.4(10.6)	8.6(1.8)
T_{2b}[s]	0.015	0.005	10^{-12}	0.0159(41)	0.0149(30)	0.0121(39)	0.0467(80)
proc. time [s]	-	-	-	0.17	8.22	18.3	1974

Table 2: Estimated parameters corresponding to the fits in figure 2 of the Iodipamide solution with the analytical and numerical models. The values correspond to the means of the posterior distributions of the estimated parameters. The values in brackets represent their standard deviations.

	prior		estimates (CW)	
parameter	mean	precision	Analytical	Numerical
M_{0b} [10^{-4}]	4.00	1.00E-12	2.63(26)	2.87(39)
k_{ba}[Hz]	900	1.00E-12	321(38)	300(47)
$\omega_{0,off}$[ppm]	0	1.00E-12	-0.153(2)	-0.16720(2)
ω_b[ppm]	5.5	1.00E-12	5.42(1)	5.43(2)
T_{2a}[s]	0.211	1.00E-12	1.59(2)	1.81(3)
T_{2b}[s]	10	1.00E-12	10(1000000)	10(1000000)

Table 3: Estimated parameters corresponding to the fits in figure 3 of Taurine solutions at different concentrations, obtained with the analytical solution.

model parameter [unit]	12.5mM	25.0mM	50.0mM	100.0mM
M_{0a} [1]	0.998(2)	0.999(1)	0.993(1)	1.002(1)
M_{0b} [10^{-4}]	2.79(18)	5.58(6)	11.59(9)	23.00(3)
k_{ba}[10^3Hz]	1.07(12)	1.79(4)	3.26(4)	6.07(8)
$\omega_{0,off}$[ppm]	-0.023(4)	0.004(2)	-0.035(2)	0.031(2)
ω_b[ppm]	2.96(3)	2.95(1)	2.96(1)	2.97(1)
T_{2a}[s]	2.0(1)	2.3(1)	2.3(2)	1.8(3)
T_{2b}[s]	20(949)	20(949)	20(949)	20(949)